X-ray scattering at liquid surfaces and interfaces

Jean Daillant

Service de Physique de l'Etat Condensé, Orme des Merisiers, CEA Saclay, F-91191 Gif sur Yvette Cedex, France
Present address: LURE, Bât 209d, Centre Universitaire Paris-sud, F-91405 Orsay Cedex, France

X-ray and neutron reflectivity techniques have become quite popular for the analysis of surfaces and interfaces over the last ten years. In this review, we discuss the specific aspects of both specular and diffuse X-ray reflectivity at liquid interfaces. We start from a model liquid surface for which the scattering cross-section can be calculated in terms of thermally excited capillary and acoustic waves, and we examine in detail the experimental consequences of the large bulk scattering and of the low q divergence of the surface scattering. Deviations from the simple calculated behaviour point to interesting phenomena which can be studied in detail, like the appearance of a bending stiffness. The method is illustrated through the discussion of representative studies of liquid surfaces, of surfactant monolayers, of liquid–liquid interfaces and of microemulsions.

1. Introduction

Reflectivity techniques are increasingly used for the study of liquid interfaces, particularly because the range of available techniques is relatively less important than for solid surfaces (no high-vacuum techniques, no scanning tunnelling microscopy, atomic force microscopy is difficult). The first experiments were carried out on liquid metals[1,2] in the seventies and on the free surface of water in the mid-eighties[3–5]. In reflectivity studies however, only density profiles averaged over the surface can be measured. From the beginning of the nineties, the analysis of diffuse scattering from the surface, which gives access to the roughness spectrum has been undertaken[6,7], where the spectrum could be measured up to wave vectors of the order of 10^7 m^{-1}. More recently, measurements at molecular length-scales could be performed[8], and the technique has now been developed to a point where very precise studies are possible over a range of length-scales spanning from angströms to tens of microns[9–11].

After an introduction to liquid interfaces, we will discuss the specific features of liquid surface reflectivity studies. We will present experimental set-ups enabling the study of horizontal surfaces. Then, using model calculations, we will discuss the subtraction of the high background scattering in the bulk liquid phases and the consequences of the low q divergence of the height–height correlation functions which make the separation of specular reflectivity and diffuse scattering impossible. The method will be illustrated through representative examples.

2. Statistical description of liquid surfaces

In this section, we first consider the microscopic structure of the interfacial region as it can be determined by a reflectivity or surface scattering experiment.

A first approach to the structure of liquid surfaces was initiated by van der Waals and consists in describing the liquid–vapour interfacial region as one of smooth transitions from the liquid density to that of the gas[12]. A complete description of van der Waals and related theories is given in Rowlinson and Widom[13]. The principle of the theory is to minimize a free energy (or grand potential) functional taking into account both the local free energy of the fluid at a given density and temperature, and the effect of density gradients (as a square gradient term in the most simple version of the theory). The minimization of this functional yields the liquid–gas interface density profile and the surface tension. This theory, however, does not properly take into account interface position fluctuations which are addressed in the alternative capillary wave theory of Buff *et al.*[14]. In its simplest version, the capillary wave theory assumes a step-like profile for the liquid–vapour interface. Then, all the structural information about the interface is contained in its profile $z(\mathbf{r}_{\parallel})$, or, since only a statistical description is meaningful, in the height correlations which are assumed to result from the propagation of capillary waves (i.e. surface deformation modes,Figure 1). There is now good experimental evidence using different

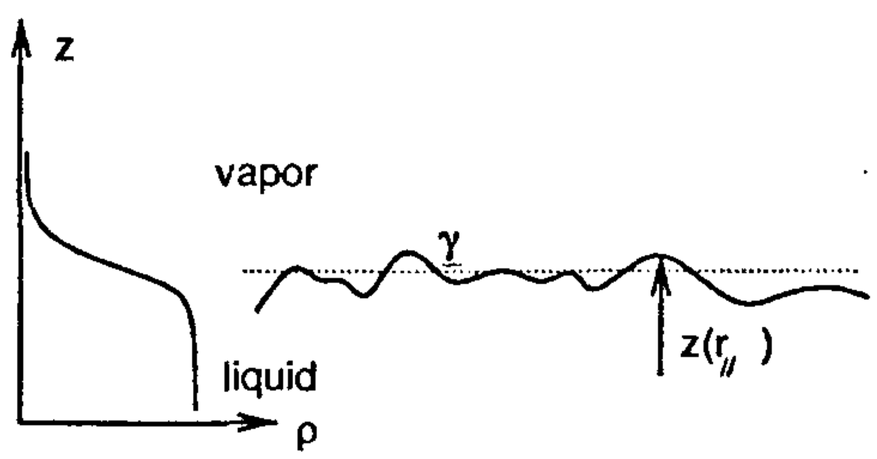

Figure 1. Capillary waves. γ is the surface tension and $z(\mathbf{r}_{\parallel})$ the interface height. The corresponding average density profile is given on the left.

e-mail: daillant@spec.saclay.cea.fr

techniques that this theory gives an accurate description of the liquid surface structure for in-plane length-scales larger than one micron, and also describes the mean surface roughness better than the van der Waals theory. We will therefore limit the discussion to its description.

2.1. *Capillary wave model*

Let $z(\mathbf{r}_\parallel)$ be the interface height at $\mathbf{r}_\parallel$ (Figure 1). The work necessary to deform the interface is:

$$W = \iint_A \mathrm{d}x\mathrm{d}y \left[\int_0^{z(x,y)} \Delta\rho g z \mathrm{d}z + \gamma\left(\sqrt{1+(\partial z/\partial x)^2+(\partial z/\partial y)^2}-1\right)\right]. \quad (1)$$

$\Delta\rho$ is the density difference between the two phases, γ the surface tension and g the acceleration of gravity. The first term describes the increase in gravitational energy for the deformed interface, and the second term the increase in free energy due to the increase in interfacial area. Developing the square root to lowest order and Fourier transforming,

$$z(\mathbf{r}_\parallel) = \sum_{q_x,q_y} z(\mathbf{q}_\parallel) e^{i\mathbf{q}_\parallel\cdot\mathbf{r}_\parallel}, \quad (2)$$

one obtains:

$$W = \gamma A + \frac{1}{2}\sum_{\mathbf{q}_\parallel}\sum_{\mathbf{q}'_\parallel} z(\mathbf{q}_\parallel) z(\mathbf{q}'_\parallel) \int_A d^2\mathbf{r} e^{i((\mathbf{q}_\parallel+\mathbf{q}'_\parallel).\mathbf{r}_\parallel)} [\Delta\rho g - \gamma \mathbf{q}_\parallel.\mathbf{q}'_\parallel], \quad (3)$$

where the modes $\mathbf{q}_\parallel = (q_x, q_y)$ are multiples of $2\pi/L$, with L a dimension of the surface of area $A = L^2$. The terms $\mathbf{q}'_\parallel \neq -\mathbf{q}_\parallel$ vanish upon integration, and

$$W = \gamma A\left\{\frac{1}{2}\sum_{\mathbf{q}_\parallel} z(\mathbf{q}_\parallel) z(-\mathbf{q}_\parallel)\left[\frac{\Delta\rho g}{\gamma}+\mathbf{q}_\parallel^2\right]\right\}. \quad (4)$$

The length $\sqrt{\gamma/\Delta\rho g}$, of the order of 1 mm is the so-called capillary length. The equipartition of energy (Gaussian–Hamiltonian) among the degress of freedom of the system in thermal equilibrium gives[15]:

$$\langle z(\mathbf{q}_\parallel) z(-\mathbf{q}_\parallel)\rangle = \frac{1}{A}\frac{k_B T}{\Delta\rho g + \gamma \mathbf{q}_\parallel^2}, \quad (5)$$

represented in Figure 2. This spectrum has been well characterized for many liquid surfaces by light scattering down to wavelengths in the micrometer range[16] and

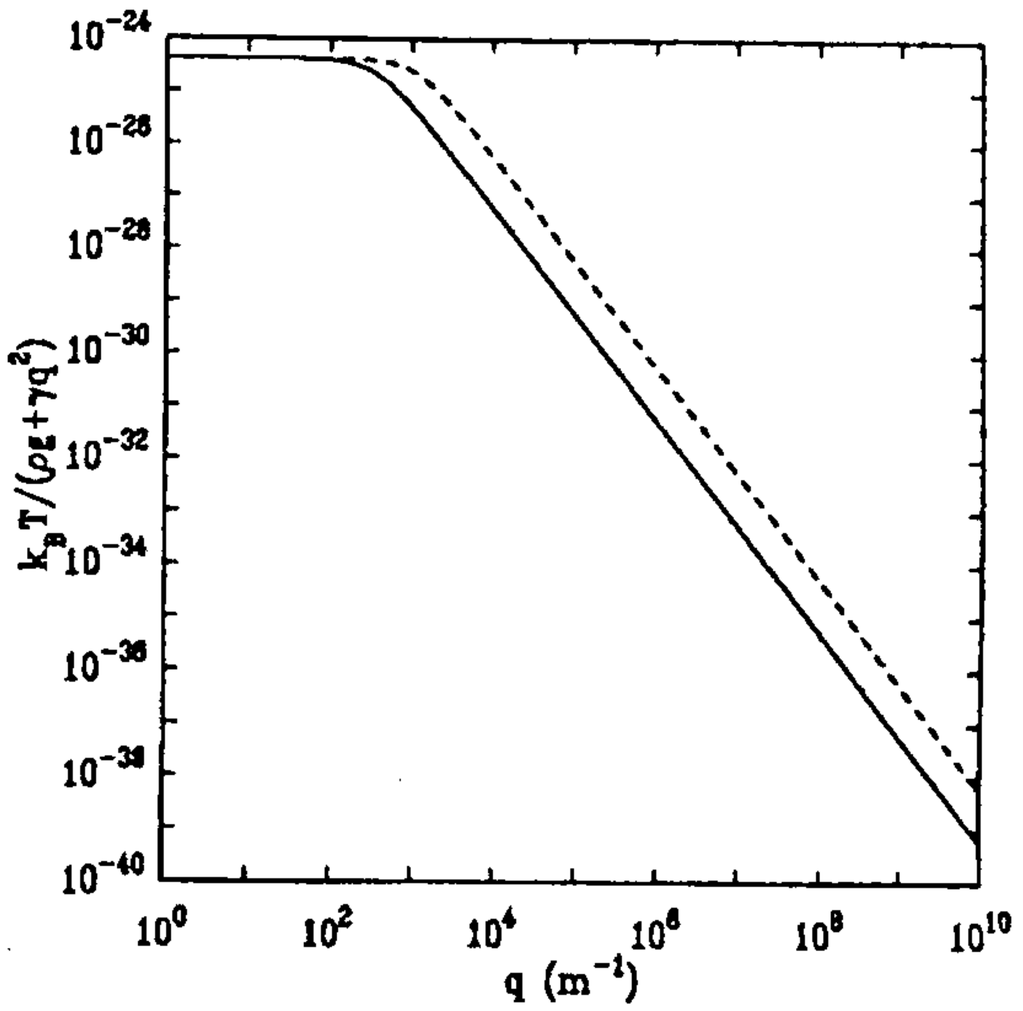

Figure 2. Amplitude of the capillary wave spectrum for surface tension $\gamma = 73$ mN/m (continuous line) and $\gamma = 7.3$ mN/m (broken line)

is valid in the limit of small in-plane momentum $\mathbf{q}_\parallel$. It describes thermally excited capillary waves, limited by gravity for length-scales larger than the capillary length, and by surface tension for smaller length-scales. The resulting surface structure is isotropic in plane.

The rms roughness of the interface is obtained by summing over all the modes:

$$\langle z^2\rangle = \frac{1}{A}\sum_{q_\parallel>0}\frac{k_B T}{\Delta\rho g + \gamma q_\parallel^2}, \quad (6)$$

where the summation runs from $q_{\min} = 2\pi/L$ to $q_{\max} = 2\pi/a$, where a is a molecular length. In the continuous limit:

$$\langle z^2\rangle = \frac{k_B T}{4\pi\gamma}\ln\left[\frac{1+q_{\max}^2(\gamma/\Delta\rho g)}{1+q_{\min}^2(\gamma/\Delta\rho g)}\right]. \quad (7)$$

Generally, we may assume $q^2{}_{\min}(\gamma/\Delta\rho g) \ll 1$ and

$$\langle z^2\rangle = \frac{k_B T}{4\pi\gamma}\ln\left[1+q_{\max}^2(\gamma/\Delta\rho g)\right]. \quad (8)$$

For $\gamma_{H_2O} = 73$ mN/m, one obtains $\langle z^2\rangle = 0.4$ nm. Also interesting are the limits:

$A \to \infty\ \langle z^2\rangle \sim -\ln g$,

$g \to 0\ \langle z^2\rangle \sim \ln A$.

These logarithmic divergences do not imply that there is no interface. The interface does exist, but is not localized in space[17], in agreement with the fact that the divergence is due to small wavevector modes $q \to 0$.

The height–height correlation function, which is important for the calculation of the scattering cross-section, can be obtained by Fourier transforming the spectrum eq. (5):

$$g(\mathbf{r}_\parallel) = \langle [z(\mathbf{r}_\parallel) - z(\mathbf{0})]^2 \rangle = 2(\langle z^2 \rangle - \langle z(\mathbf{0}) z(\mathbf{r}_\parallel) \rangle), \tag{9}$$

with

$$\langle z(\mathbf{0}) z(\mathbf{r}_\parallel) \rangle = \frac{k_B T}{2\pi\gamma} K_0(r_\parallel \sqrt{\Delta\rho g/\gamma}). \tag{10}$$

K_0 is the modified second-kind Bessel function of order 0. $K_0(x)_{x \to 0} \simeq \log 2 - \gamma_e - \log x$ and $\lim K_0(x)_{x \to \infty} = 0$.

Equation (5) gives a good description of liquid surfaces at scales larger than a few nm (see later in the article), and studying deviations from eq. (5) will allow a detailed understanding of the underlying physical processes like phase transitions in a surfactant film and surface buckling[18]. A first open question is that of the corrections to the surface energy of a simple liquid at very small length-scales. Going to such small scales of the order of a few molecular diameters, it will no longer be possible to unambiguously distinguish betwen interface position fluctuations and density fluctuations, and the simple capillary description eq. (5) will certainly break down. Also, the lowest order development leading to eq. (3) will no longer be valid and higher order terms will appear, resulting in a wavevector-dependent surface tension. Explicit renormalization calculations[19] show that the effective surface tension at very short length-scales is larger than the macroscopic surface tension. The opposite trend is displayed when we take into account the effect of long-range dispersion forces which lead to a smaller effective surface tension[20].

If now a film is present at the interface, it will reduce the surface tension but also resist bending. The simplest treatment of these effects which will be most important for very low surface tensions, is due to Helfrich[21], and is described here. Very low surface tensions can be achieved, for example in microemulsions composed of brine, oil (e.g. alkanes) and surfactants where interfacial tensions as low as a few thousandths of a mN/m can sometimes be obtained. In such systems fluctuations play an important role. This, for example, is the case of lamellar phases which can be diluted down to very low concentrations where the separation between lamellae (> 100 nm) is larger than the range of electrostatic forces. Such structures are stabilized by the so-called Helfrich entropic interaction (undulation forces): the fluctuations of a lamella are limited by the neighbouring lamellae, resulting in a repulsive effective interaction. For such systems having a very low surface tension, the fluctuations are no longer limited by the surface tension but by the bending stiffness. In general, the description of the surface curvature requires two parameters independent of the surface parameterization, the mean curvature and the Gaussian curvature. However, the integral of the Gaussian curvature over the surface is a constant if there is no change of topology (Gauss theorem), and only the mean curvatuve, which can be approximated as $\sqrt{(\partial^2 z/\partial x^2)^2 + (\partial^2 z/\partial y^2)^2}$ to lowest order, has to be retained for a planar film. If the sign of the curvature is assumed to be unimportant for a film without spontaneous curvature, bending stiffness can then be taken into account by an additional term proportional to the square of the mean curvature in eq. (1):

$$\int\int \mathrm{d}x\mathrm{d}y\kappa \left[\left(\frac{\partial^2 z}{\partial x^2} \right)^2 + \left(\frac{\partial^2 z}{\partial y^2} \right)^2 \right],$$

where κ is the bending rigidity modulus. Methods similar to those previously used now lead to:

$$\langle z(\mathbf{q}_\parallel) z(-\mathbf{q}_\parallel) \rangle = \frac{1}{A} \frac{k_B T}{\Delta\rho g + \gamma q_\parallel^2 + \kappa q_\parallel^4}. \tag{11}$$

A comprehensive understanding of the bending rigidity in terms of molecular order and chain conformations is still lacking.

2.2. *Scattering by capillary waves*

Under the Born approximation which is the simplest approximation used for the treatment of surface scattering (scatterers only 'see' the incident radiation, and there is no multiple scattering), the scattering cross-section can be written:

$$\frac{\mathrm{d}\sigma}{\mathrm{d}\Omega} = r_e^2 (\hat{\mathbf{e}}_{in} \cdot \hat{\mathbf{e}}_{sc})^2 \left| \int \mathrm{d}\mathbf{r} \rho_{el}(\mathbf{r}) e^{i\mathbf{q}\cdot\mathbf{r}} \right|^2, \tag{12}$$

where $r_e = 2.818 \times 10^{-15}$ m is the classical electron radius which is the scattering length for electrons, ρ_{el} is the electron density of the medium, $\mathbf{q}$ is the wavevector transfer, and $\hat{\mathbf{e}}_{in}$ and $\hat{\mathbf{e}}_{sc}$ are the polarization vectors of the incident and scattered fields. Integrating over z and averaging over the surface[22], one obtains for the scattering by a rough surface of dimensions L_x and L_y along O_x and O_y, whose correlations are described by $g(\mathbf{r}_\parallel) = 2\langle z^2 \rangle - 2\langle z(\mathbf{0}) z(\mathbf{r}_\parallel) \rangle$:

$$\frac{\mathrm{d}\sigma}{\mathrm{d}\Omega} = \frac{\rho_{el}^2 r_e^2 L_x L_y}{q_z^2} (\hat{\mathbf{e}}_{in} \cdot \hat{\mathbf{e}}_{sc})^2 \int \mathrm{d}\boldsymbol{\eta}_\parallel e^{i\mathbf{q}_\parallel \cdot \boldsymbol{\eta}_\parallel} e^{-\frac{1}{2} q_z^2 g(\boldsymbol{\eta}_\parallel)}, \tag{13}$$

where q_z and $\mathbf{q}_\parallel$ are the wavevector transfer components normal and parallel to the surface, respectively. For

scattering of a (s) polarized wave, (i.e. normal to the plane of incidence) into a (s) polarized wave, $\hat{\mathbf{e}}_{in} \cdot \hat{\mathbf{e}}_{sc} = \cos\psi$, the angle between the incident and scattered beams. Looking at eq. (13), two cases may happen: the integral may exist, or may not. Only for fast decreasing $\exp(-1/2q^2{}_z g(\mathbf{r}_\parallel))$, i.e. slowly decreasing $g(\mathbf{r}_\parallel)$ or long-range height correlations, will the integral exist. In that case, $d\sigma/d\Omega$ is a function and there is no specular reflection. This would be the case for the liquid surfaces if the logarithmic divergence with distance in the correlation function were not to be limited by gravity or finite size. For fast enough decreasing correlations on the contrary, the scattering cross-section can be separated into a specular and a diffuse part by writing:

$$e^{q_z^2\langle z(\mathbf{0})z(\mathbf{r}_\parallel)\rangle} = 1 + \left(e^{q_z^2\langle z(\mathbf{0})z(\mathbf{r}_\parallel)\rangle} - 1\right),$$

where 1 gives the specular contribution (its Fourier transform is proportional to $\delta(\mathbf{q}_\parallel)$), and the term within parenthesis gives the diffuse scattering.

In fact, the Born approximation is generally not a good enough approximation, in particular under total external reflection condition. Total external reflection occurs for X-rays for grazing angles of incidence below a critical angle $\theta_c = \sqrt{2(1-n)} \approx 10^{-3}$ since the optical index is slightly less than 1. In this region, the so-called distorted-wave Born approximation (DWBA) which still only considers single *diffuse* scattering events but treats reflection rigorously can be used. Within this approximation, the generalization of eq. (13) is (for the diffuse part):

$$\frac{d\sigma}{d\Omega} = A\frac{k_0^4}{16\pi^2}(n_1^2 - n_0^2)^2 |t_{0,1}^{in}|^2 |t_{0,1}^{sc}|^2 \frac{e^{-\frac{1}{2}(q_{z,1}^2 + q_{z,1}^{*2})\langle z^2\rangle}}{|q_{z,1}|^2} \times \cos^2\psi \int d\mathbf{R}_\parallel \left[e^{|q_{z,1}|^2\langle z(\mathbf{R}_\parallel)z(\mathbf{0})\rangle} - 1\right] e^{i\mathbf{q}_\parallel\cdot\mathbf{R}_\parallel}, \quad (14)$$

where $t_{0,1}^{in}$ and $t_{0,1}^{sc}$ are the Fresnel transmission coefficients between the upper (0) and lower (1) media of indices n_0 and n_1 for polarization (s) for the angle of incidence θ_{sc}, respectively and $q_{z,1}$ is the normal component of the wavevector transfer in medium 1. Equation (14) differs from eq. (13) by the additional transmission coefficients. This expression is explicitly symmetrical in the source and detector positions as required by the reciprocity theorem. At the critical angle for total external reflection $\theta_{in} = \theta_c$, the transmission coefficients in eq. (14) have a peak value of 2. The electric field is then at its maximum value at the interface because the incident and scattered fields are in phase at $z = 0$. There is a maximum in the scattered intensity known as Yoneda peak.

Substituting eq. (9) into eq. (14), it is possible to find the expression of the scattered intensity. Particularly useful is the following approximation for the scattering cross-section which is valid in the limit $q_\parallel \gg \sqrt{\Delta\rho g/\gamma}$ (refs 7, 22–24):

$$\frac{d\sigma}{d\Omega} \approx \mathcal{A}\frac{k_0^4(1-n^2)^2}{16\pi^2}|t_{0,1}^{in}|^2 |t_{0,1}^{sc}|^2 \frac{k_B T}{\gamma q_\parallel^2}\left(\frac{q_\parallel}{q_{max}}\right)^\eta, \quad (15)$$

where $\mathcal{A}$ is the illuminated area and $\eta = (k_B T/2\pi\gamma)|q_{z,1}|^2$.

3. Experimental measurement of the reflectivity of liquid surfaces

3.1. *Specular reflectivity*

Considering the measurement of the reflectivity of liquid surfaces, we first note that the liquid surface must necessarily be horizontal. If the X-ray source is a sealed tube, it can be moved to change the angle of incidence, whereas using a rotating anode or synchrotron radiation sources alternative solutions must be considered. The angular spread of a rotating anode source can be used to change the incidence on a fixed point by displacing a monochromator on a circle containing the source and the target point (Figure 3).

Using synchrotron radiation, two different solutions have been found. For grazing incidence a mirror is generally used. For higher incidences, a crystal deflector can be used (Figure 4) to deflect the beam[22], for

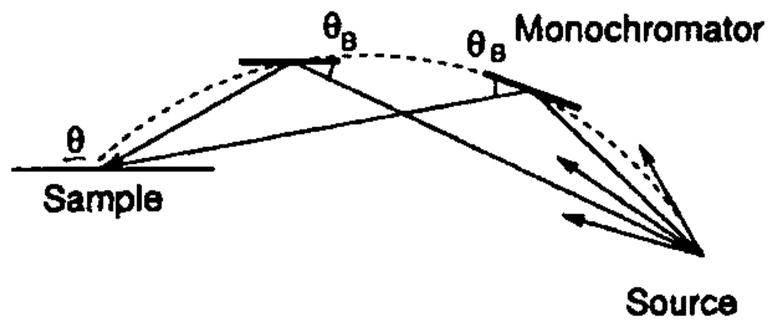

Figure 3. Experimental set-up for changing the angle of incidence at a fixed point using a divergent X-ray source, e.g. a rotating anode. The monochromator is moved on a circle containing the source and target point.

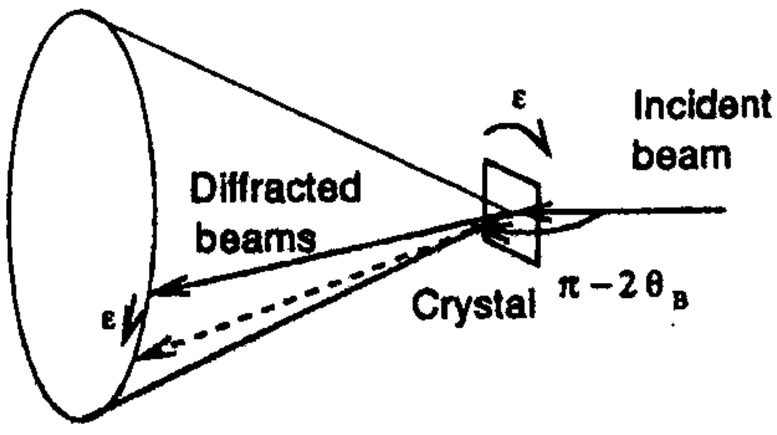

Figure 4. Beam deflector. By rotating the crystal around the incident beam, the diffracted beam describes a cone of opening angle $4\theta_B$ if θ_B is the Bragg angle.

example a very thin silicon crystal. By rotating the crystal around the incident beam, the diffracted beam describes a cone of opening angle $4\theta_B$ if θ_B is the Bragg angle. The whole diffractometer must then be moved to keep a fixed point of impact. This crystal can be bent to fit the divergence requirements of the incident beam.

Another crucial experimental problem posed by reflectivity measurements on liquid surfaces is that of the background due to scattering in the bulk. If one is interested in specular reflectivity, the most efficient method could at first sight consist in scanning in q_x for each q_z value in order to determine and subtract the background. In fact, this is always ambiguous, since as a consequence of the long-range correlations, the diffuse intensity is generally peaked in the specular direction for liquid surfaces, as shown in Figure 5 (ref. 18). The contribution of diffuse scattering within resolution limited specular peak must always be taken into account in the analysis.

This is illustrated in Figure 6. In that case, we calculated expected intensity from a rough surface having a height–height correlation given by eq. (11) measured in the specular direction for a resolution Δq_x in the plane of incidence to be smaller than the reflectivity of an equivalent smooth interface by a factor

$$\pi^{-1/2}\Gamma\left[\frac{1}{2}-\frac{k_BTq_z^2}{4\pi\gamma},\frac{1}{2}\Delta q_x^2\frac{\kappa}{\gamma}\right] \times \exp-\left[\frac{k_BTq_z^2}{2\pi\gamma}\log\left(\frac{e^{\gamma_E}}{\sqrt{2}}\sqrt{\frac{\gamma/\kappa}{\Delta q_x}}\right)\right], \quad (16)$$

where Γ is the incomplete Γ function and $\gamma_E = 0.577$ is Euler's constant. This factor is larger than $e^{-q_z^2\langle z^2\rangle}$ which corresponds to the attenuation of the truly reflected (specular) intensity, because the contribution of diffuse scattering has been taken into account in addition to specular reflectivity. One can see in Figure 6 that this diffuse contribution dominates the specular intensity for $q_z > 2$ nm^{-1}. Note also that a data analysis not taking into account diffuse scattering leads to an erroneous estimation of the structural parameters.

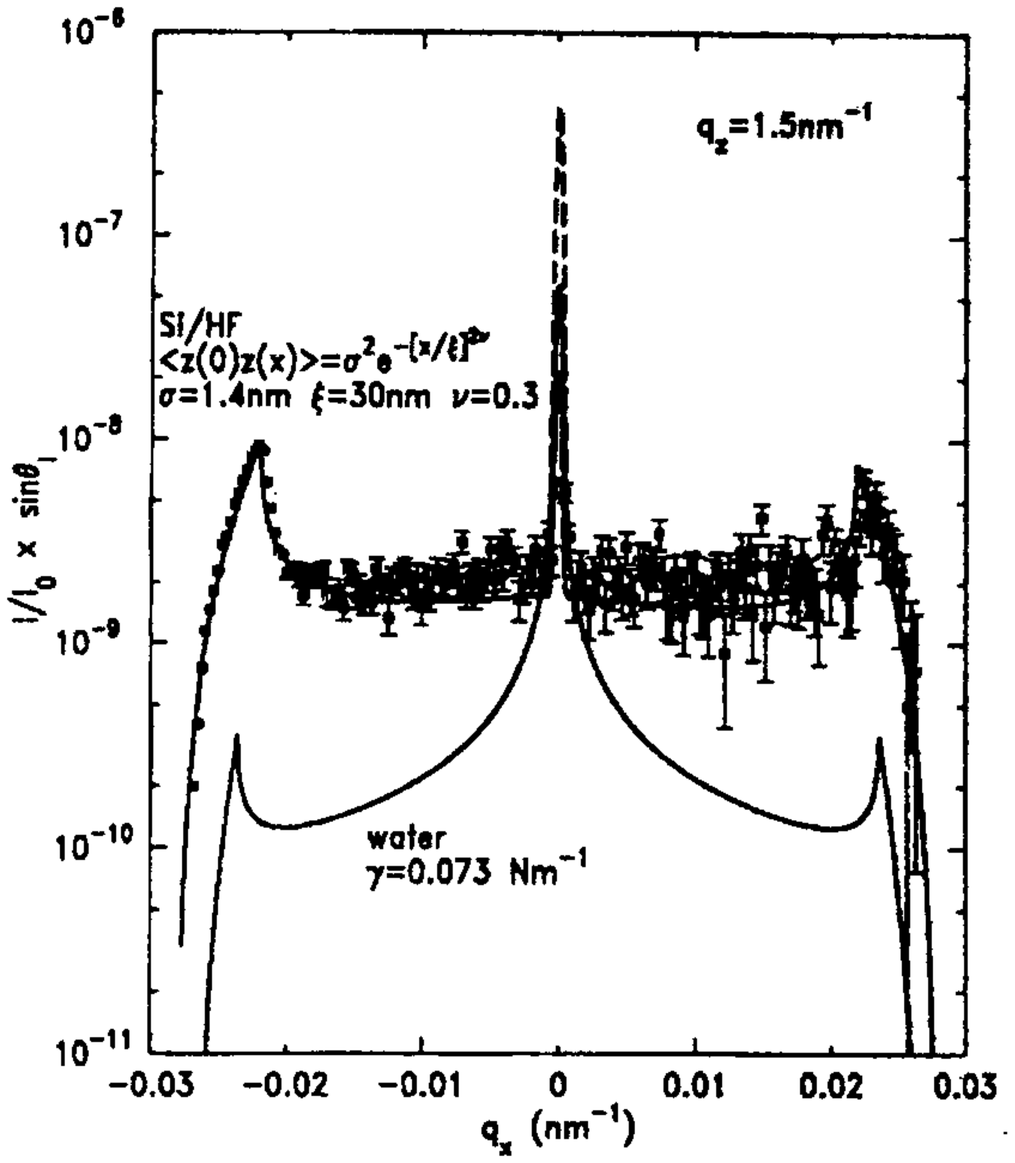

Figure 5. Diffuse scattering from the bare water surface (calculated) and a solid surface.

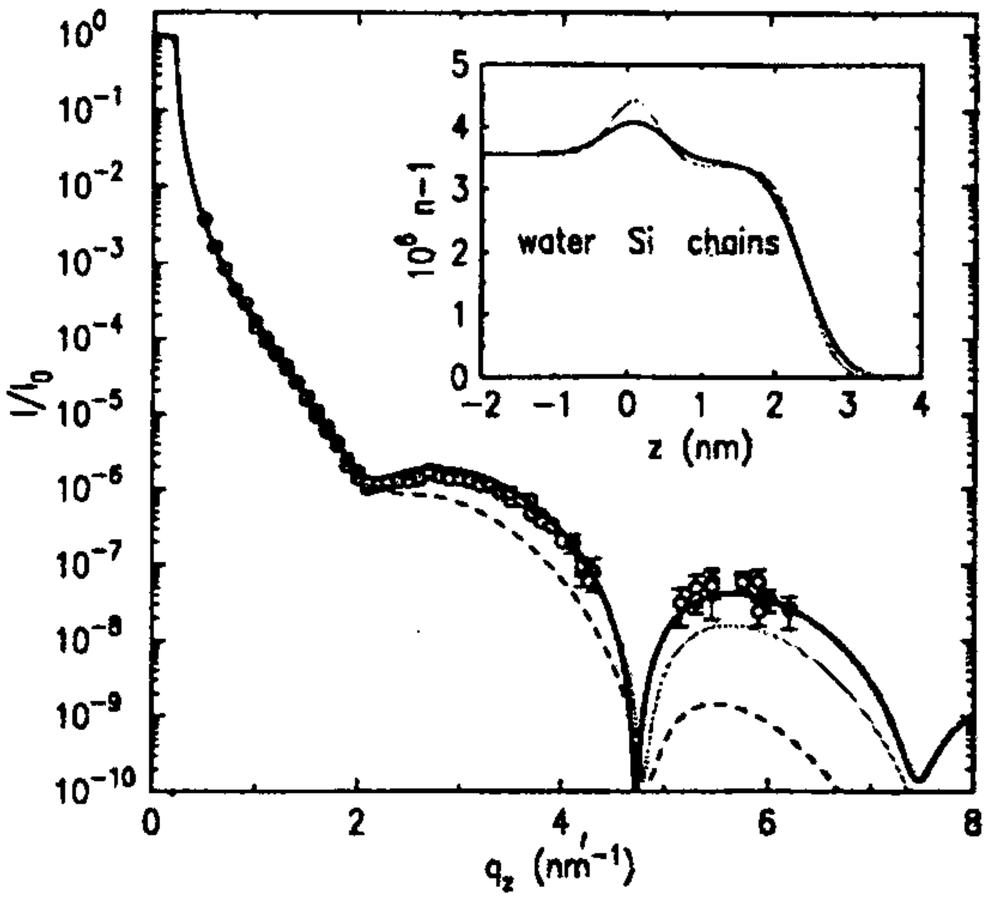

Figure 6. Interference pattern resulting from the reflection of an X-ray beam on an octadecyltrichlorosilane monolayer at the air/water interface and its corresponding electron density model (inset, black curve). The broken curve represents the specular reflection, the long-dashed curve the diffuse intensity, and the thick line the total intensity. The faint curve in the inset is obtained when the data are analysed using a 'box model' with error function transition layers, not taking into account diffuse scattering.

3.2. *Diffuse scattering*

The case of diffuse scattering is even more difficult. One would expect that the same kind of measurements that are successfully carried out on solid surfaces could be also applied to liquid surfaces, and in particular, 'rocking curves' (equivalent to q_x scans at fixed q_z)[26,27]. In fact, bulk scattering in the liquid phase dramatically increases if both the angle of incidence and the scattering angle become larger than the critical angle for total external reflection, and it is in practice necessary to fix the incidence angle below θ_c if one wants to measure the small scattering at short length-scales (the scattering decays at least as $q^{-2}_{\parallel}$). It is then possible to measure the scattered intensity either in the plane of incidence

(projected on q_x) or in the horizontal sample plane. In the first case, q_x and q_z are varied together (Figure 7) and it is possible to measure the normal structure of, for example, a film, and verify that surface scattering is indeed measured. However, one has to decouple the structural effects from the fluctuation spectrum. Measuring diffuse scattering in the plane of incidence should be considered whenever one is interested in the determination of the normal structure of thin films using synchrotron radiation. This has two main advantages over reflectivity (see Figure 8): (i) The reduced background; (ii) The much lighter experimental set-up (only a mirror is required instead of a beam deflector).

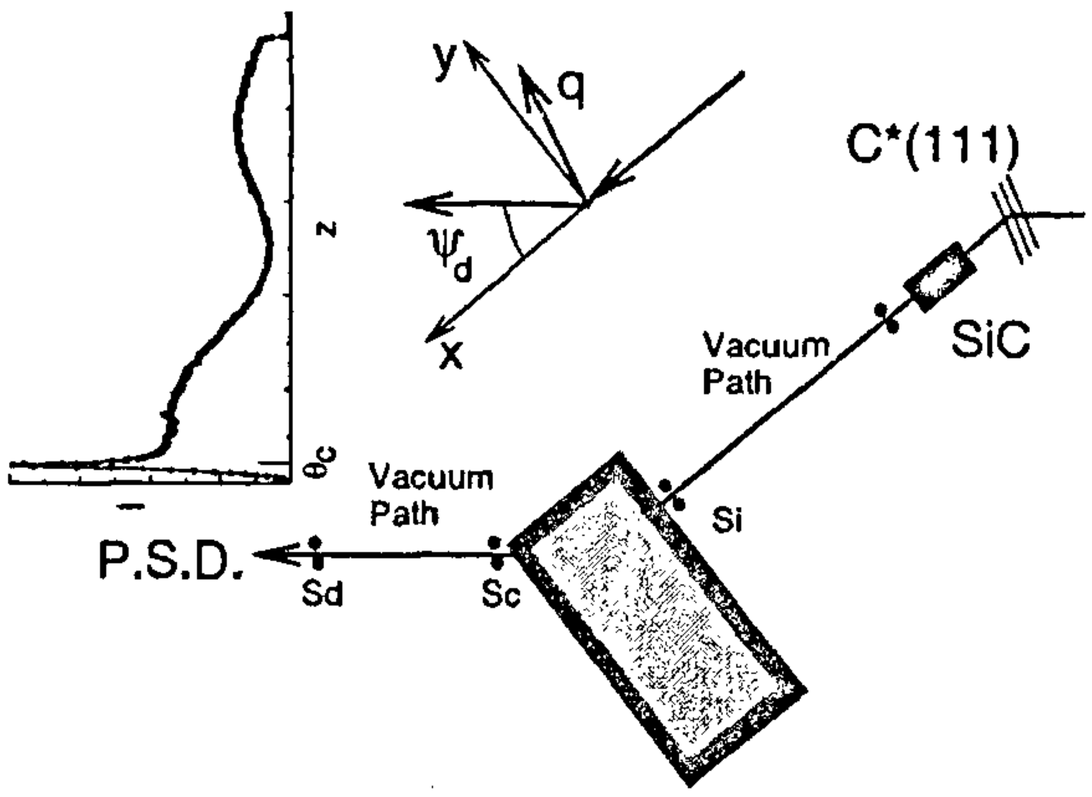

Figure 9. Schematic of experiments (Troika beamline, ESRF), in-plane q_y geometry; C^* (111), diamond monochromator; SiC, mirror; PSD, position sensitive gas-filled (xenon) detector. The experimental curve represents the scattered intensity as a function of the vertical position on the PSD. Typical distances are: Sample to S_d distance 700 mm; S_c–S_d distance 500 mm. Typical horizontal × vertical openings of the slits S_i, S_c and S_d are $w_i \times h_i$: 0.3 mm × 0.2 mm; $w_c \times h_c$: 0.3 mm × 100 mm, $w_d \times h_d$: 0.5 mm × 100 mm.

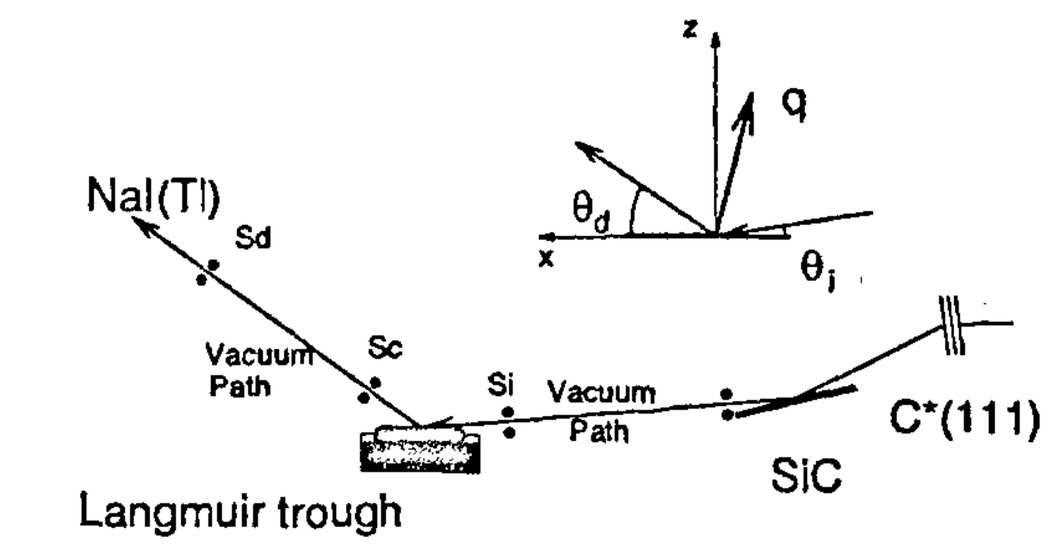

Figure 7. Schematic of experiments (Troika beamline, ESRF). (q_x, q_z) plane of incidence geometry; in-plane q_y geometry; C^* (111), diamond monochromater; SiC, mirror; NaI (Tl), scintillation detector. Typical distances are: Sample to S_d distance 700 mm; S_c–S_d distance 500 mm. Typical horizontal × vertical openings of the slits S_i, S_c and S_d are $w_i \times h_i$: 0.4 mm × 0.2 mm; $w_c \times h_c$: 2 mm × 2 mm; $w_d \times h_d$: 10 mm × 0.250 mm.

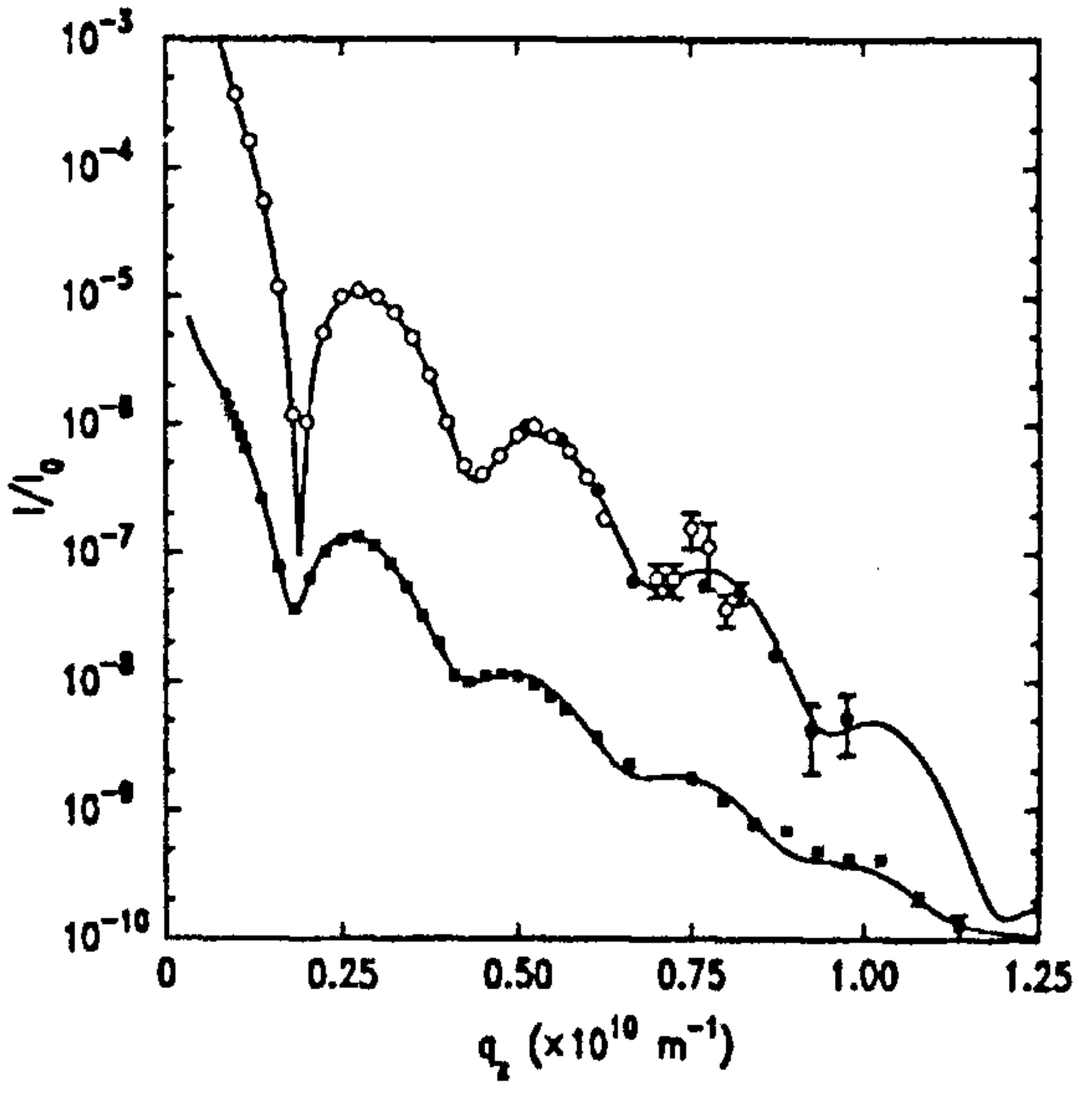

Figure 8. Laboratory (empty circles) and synchrotron (filled circles) reflectivity experiments (top). Diffuse scattering experiment in the plane of incidence (filled squares, bottom) for the same arachidic acid monolayer on a $CdCl_2$ subphase.

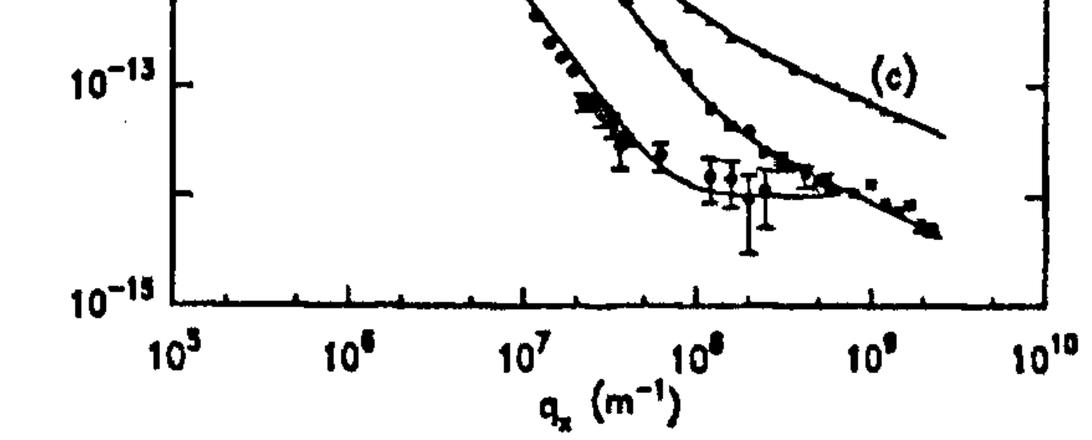

Figure 10. Resolution effect for scans in the plane of incidence. (a) The scattered intensity depends on the height of the sample S_c and detector slit S_d. If both heights are multiplied by a factor of 2, the intensity is multiplied by a factor of 4 (2 for the illuminated area and 2 for the angular acceptance); (b) Closing S_c (inverted triangles) introduces a cut-off in the resolution functions (these curves have been divided by 100, and the diamonds indicate the background); (c) Closing the slits in the plane of the sample limits the horizontal integration of the spectrum (curves divided by 10^4).

When we are only interested in the roughness spectrum, a second kind of scan (in the horizontal sample plane) which directly yields a signal proportional to the roughness spectrum should be preferred (Figure 9).

A last important point which is not specific to liquid surfaces is that the diffuse intensity is proportional to the resolution volume (Figure 10). It is therefore necessary to precisely determine the resolution function as a function of slit openings and of the footprint of the beam on the surface to precisely determine the magnitude of this intensity.

4. Some examples

4.1. *Simple liquid-free surface*

The bare water-free surface was studied for the first time by Braslau *et al.*[3] at Hasylab, Hamburg (Figure 11, left). Their results were successfully interpreted within the frame of the capillary wave model and they found a rms roughness $\langle z^2 \rangle = 0.32$ nm. These results have been confirmed and improved in Braslau *et al.*[4] and Daillant *et al.*[5]. In Schwartz *et al.*[6] diffuse scattering from the surface was also measured, and it was demonstrated that the capillary wave model could be applied down to distances as small as 50 nm. This model was applied in Sanyal *et al.*[7] for the ethanol surface up to wave vectors of the order of 10^7 m^{-1} (Figure 11, right).

In both cases, the limit was fixed by the source flux and background subtraction. This is not longer the case for the experiments carried out at the European Synchrotron Radiation Facility[8]. The intensity scattered in the plane of incidence is presented in Figure 12 *a*. The data extend to $q \geq 10^8$ m^{-1} and are well described by the capillary wave spectrum. The data taken in the interface plane (Figure 12 *b*) extend to even larger wave vectors $\approx 10^{10}$ m^{-1}, note that this is more than two orders of magnitude than that of the best previous measurements[6] but can only be described with the spectrum of eq. (5) up to $q \approx 5 \times 10^8$ m^{-1}. The excess scattering at $q \geq 10^9$ m^{-1} could indicate either a smaller effective surface tension at such large wavelenghts[20] or another source of scattering. This scattering has no measurable dependence on q (the apparent q^{-1} dependence in Figure 12 is due to the resolution function), and can be attributed to density fluctuations (acoustic waves) within the penetration depth of the beam.

The corresponding scattering cross-section[22] can be calculated from the density–density correlation function at or near the interface which can itself be determined by using the linear response theory[16]:

$$\frac{d\sigma}{d\Omega} = \frac{k_0^4}{16\pi^2} \frac{A(1-n^2)^2 |t_{0,1}^{in}|^2 |t_{0,1}^{sc}|^2 k_B T \kappa_T}{2Im(q_{z,1})}, \qquad (17)$$

where n is the refractive index of water, $t_{0,1}^{in}$ and $t_{0,1}^{sc}$ are the transmission coefficients of the air/water interface for the incident and scattered beams, κ_T is the isothermal compressibility of water (4.58×10^{-10} m^2 N^{-1}), and

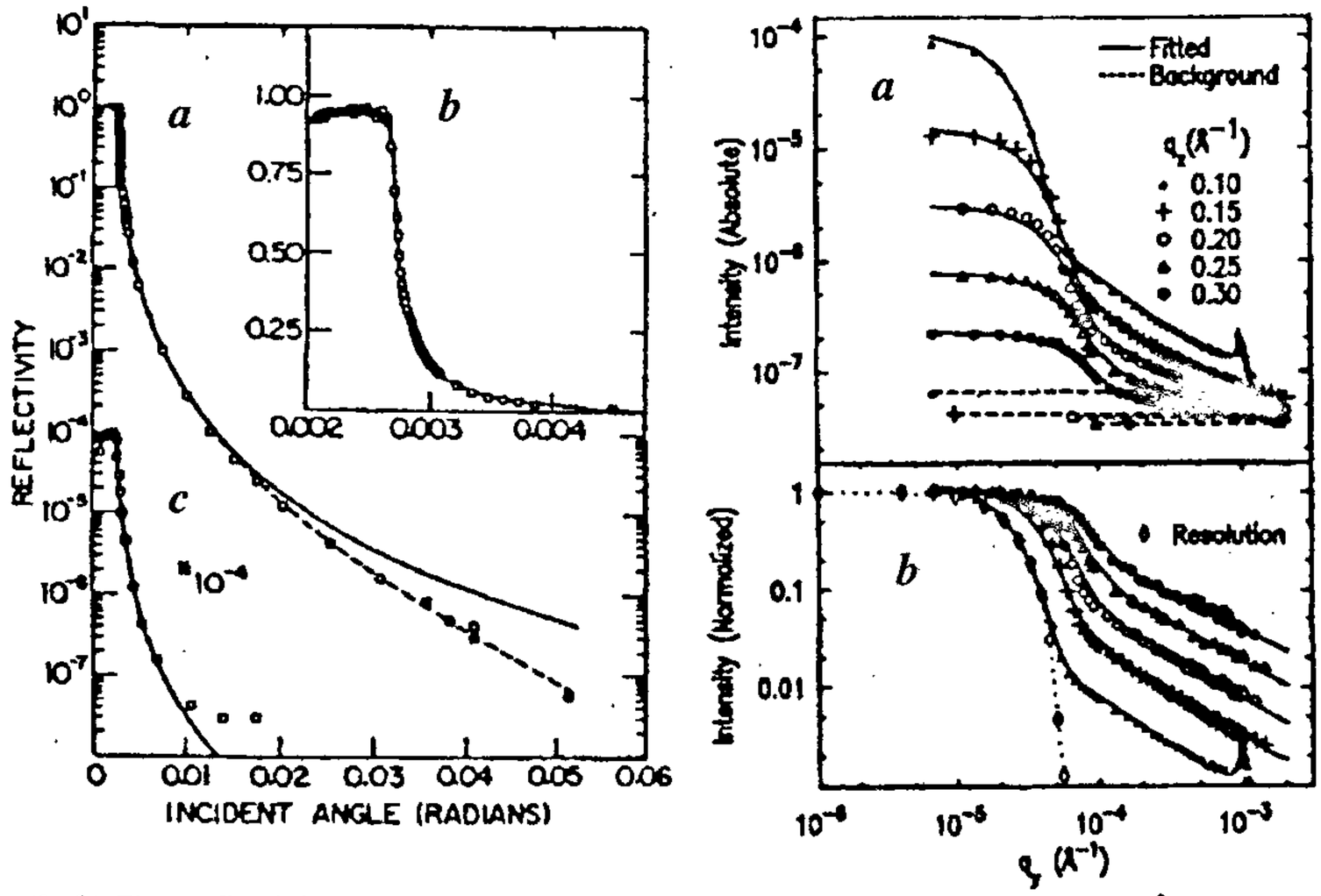

Figure 11. (Left) First reflectivity experiment on the bare water-free surface by Braslau *et al.*[3] at Hasylab. ***a***, Measured X-ray reflectivity (circles), calculated Fresnel reflectivity (continuous line); the dotted line takes the capillary wave roughness into account; ***b***, Expanded version around the critical angle for total external reflection; ***c***, Same as ***a*** but measured using a rotating anode generator. (Right) ***a***, Diffuse scattering by the ethanol-free surface (Sanyal *et al.*[7], NSLS beamline X22B). q_x scans at constant q_z; The background is subtracted in ***b***.

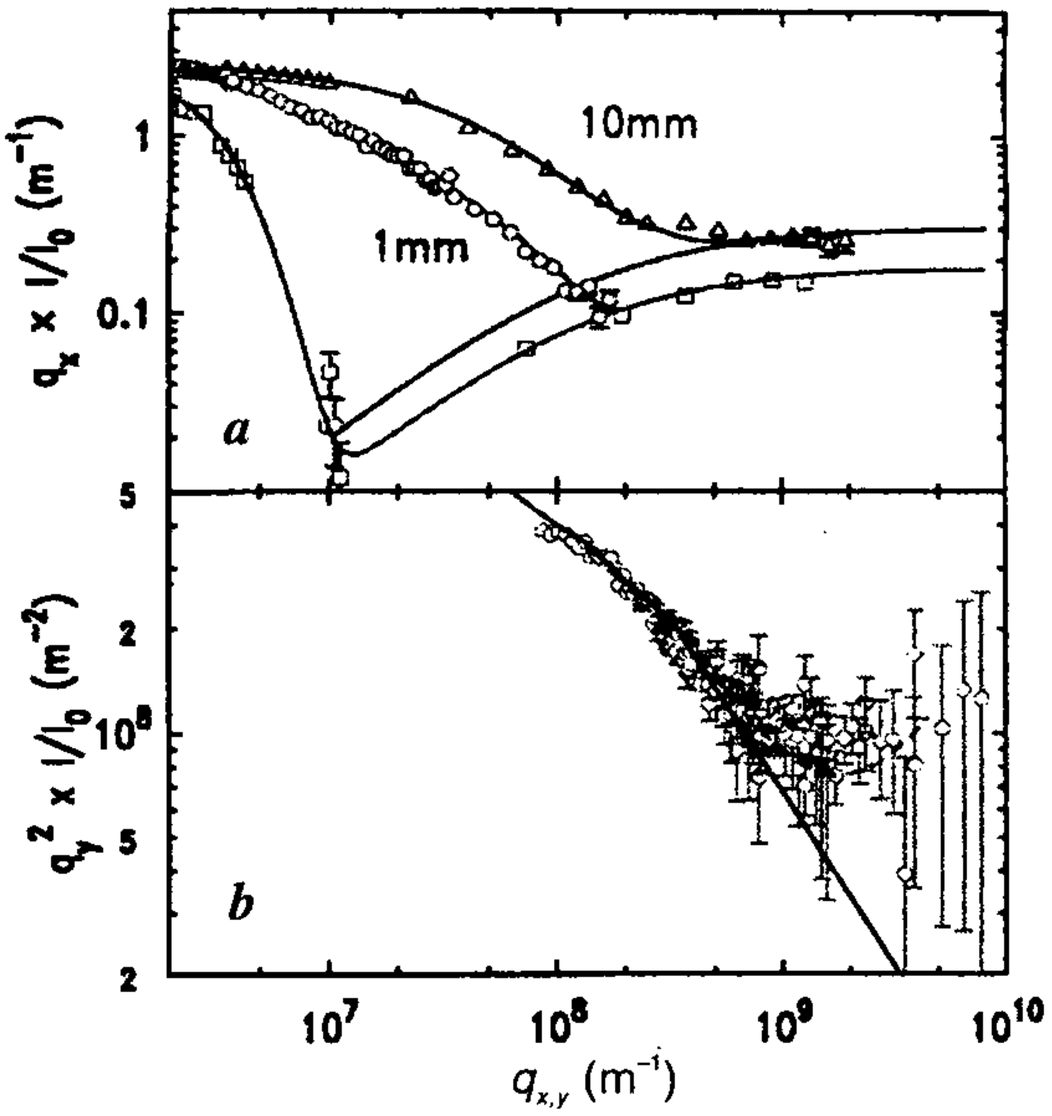

Figure 12. Scattering by the bare water surface in the plane of incidence (*a*) and in the plane of the surface (*b*). For measurements in the plane of incidence q_x is the projection of the wave vector transfer on the horizontal. 1 mm (circles) and 10 mm (triangles) are the openings of slit S_c in Figure 7. Squares represent the background which was not subtracted. In *b*, the background was subtracted following the procedure indicated in text. The full line is calculated by using the capillary wave spectrum and the acoustic wave scattering cross-section eq. (17) has been included to calculate the dashed line curve. Note that the great dynamic range of the *y*-scale has been compressed by a multiplication of the measured scattered intensity by q_x or q_y^2.

$\mathcal{I}m(q_{z1})$ is the imaginary part of the normal component of the wave vector transfer in the liquid (inverse of the penetration length). Including this contribution gives a better agreement (Figure 12 *b*), without discarding the possibility of other corrections.

Alcohol and alkane surfaces have also been extensively studied[28]. In particular, wetting of the liquid phase by a crystal phase has been discovered.

4.2. *Surfactant monolayers*

Surfactant monolayers have been the subject of many X-ray and neutron reflectivity studies. We shall only discuss one of them to illustrate the manner in which information can be extracted from a reflectivity experiment. A very comprehensive study of long-chain alcohols ($C_{10} \rightarrow C_{16}$) at the air/water interface has been carried out by Rieu *et al.*[29] (Figure 13). From their very precise measurements, the authors were able to measure the density of both the aliphatic chains and of the headgroups as a function of temperature. The data were sufficiently well resolved to evidence thickness and density changes at a two-dimensional liquid–solid (rotator phase) transition (Figure 13). The bending rigidity modulus was also evaluated. Such a determination is necessarily very rough in a reflectivity experiment, but when a surfactant monolayer is present at the interface, its first effect is indeed to reduce the surface tension: $\gamma = \gamma_{H_2O} - \Pi$, where Π is the surface pressure, as illustrated in Figure 14 for an arachidic acid (CH_3 –

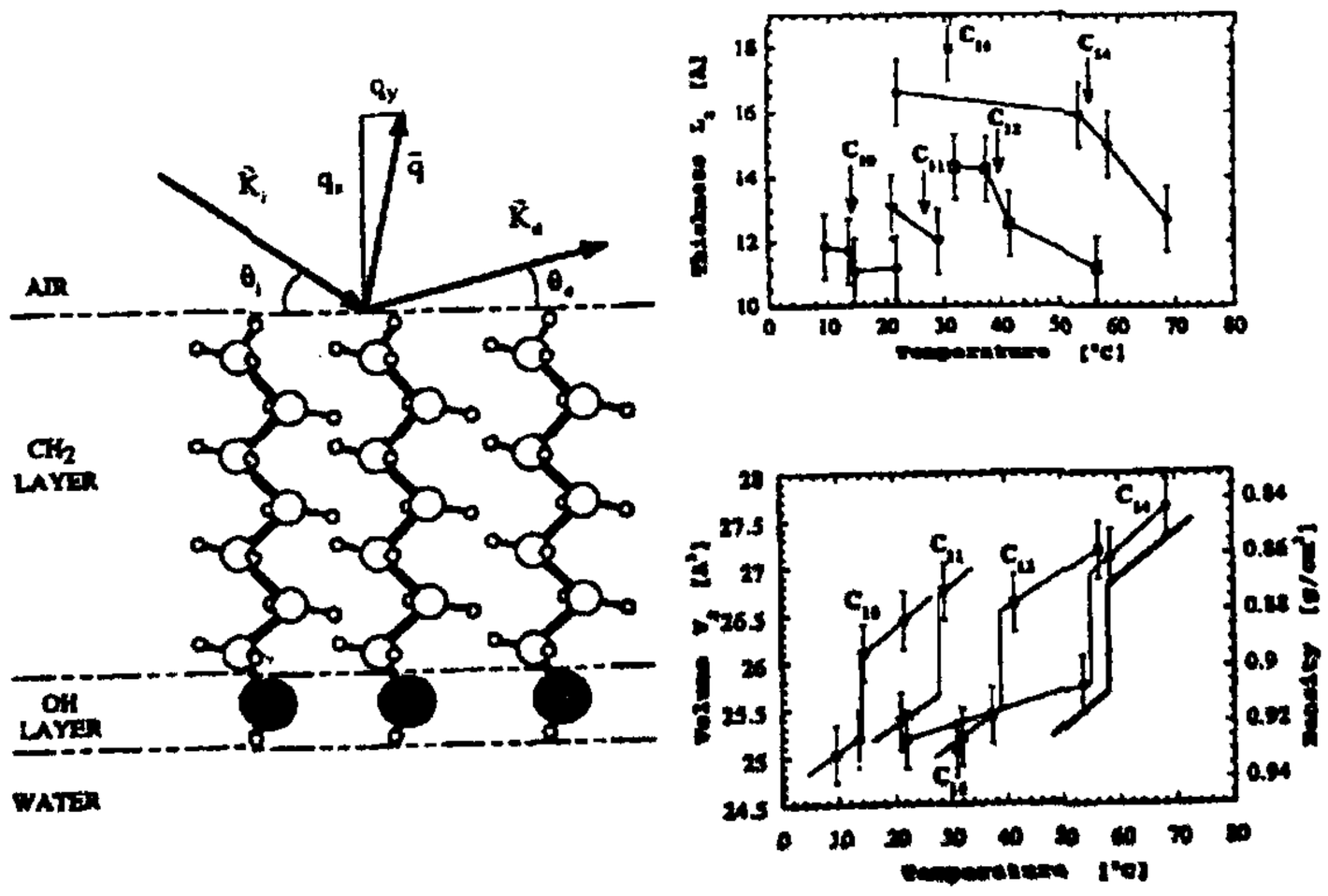

Figure 13. (Left), Schematic of the alcohol monolayer at the air/water interface. (Top, right), Film thickness as a function of temperature. The arrows indicate the phase transition. (Bottom, right), Volume per CH_2 as a function of temperature. Note the density jump at the 2D liquid to solid (rotator phase) transition. Adapted from Rieu *et al.*[29].

$(CH_2)_{18} - COOH$) film. However, higher order corrections to the spectrum, i.e. effects of the bending stiffness of the film can also be evidenced. Results for a L_α dipalmitoylphosphatidyl choline (DPPC) film on pure water are presented in Figure 15. Whereas at small q_y values the scattered intensity scales with the surface tension as expected, this is no longer true at large q_y due to the effect of bending stiffness.

The data in Figure 15 have been analysed using the spectrum eq. (11) including the additional term $\kappa_q{}^4$ in the denominator. For the more compressed film in Figure 15 it is found that $\kappa = (5 \pm 2)k_BT$, smaller than generally expected in condensed DPPC films[30]. The observed wave vector range is not large enough to allow the precise determination on the exponent 4. Smaller exponents are however found with the very rigid films[8] formed by fatty acids (here behenic acid $CH_3 - (CH_2)_{20} - COOH$) on divalent cation subphases (5×10^{-4} mol/l $CdCl_2$) at high pH (8.9) and low temperature (5°C). Uncompressed, such films exhibit a $q^{-3.3}$ power law which has been attributed to the coupling between in-plane (phonons) and out-of-plane elasticity[8]. Finally, in systems with more than one interface, it is possible to measure the correlation between the interfaces. This is the case for soap films[31] and also for free-standing smectic films for which the elastic constants can be measured[32].

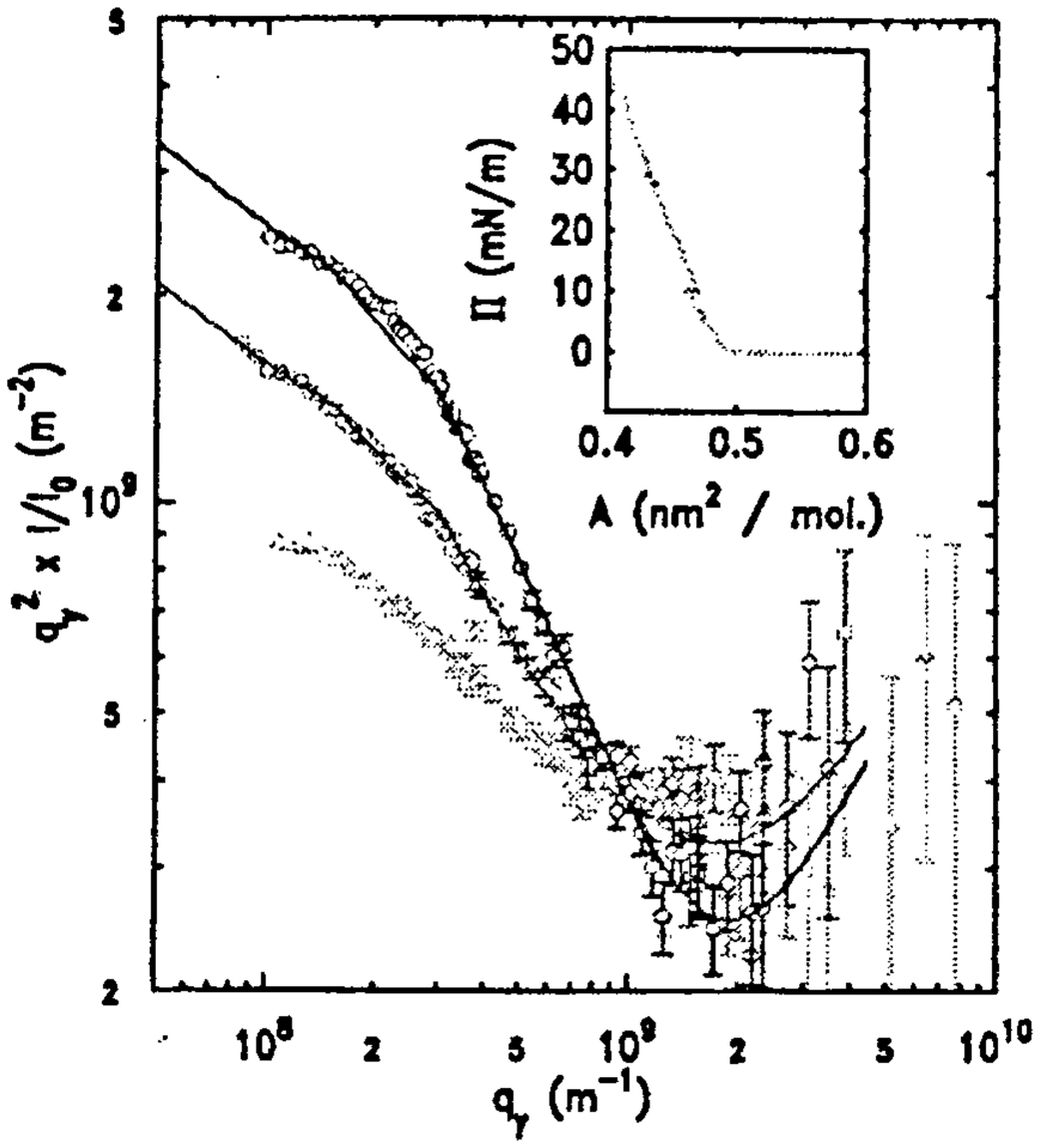

Figure 15. Intensity scattered in the horizontal plane by a bare water surface (light triangles) and a DPPC film at 3°C compressed at 20 mN/m (light circles) and 40 mN/m (dark circles). Lines are the best fits as indicated in text. Note that the scattered intensity scales with the surface tension at low q_y but that this is no longer true at large q_y due to the effect of bending stiffness (the dark curve passes below the light curves). (Inset), corresponding molecular area–surface pressure isotherm of the DPPC film.

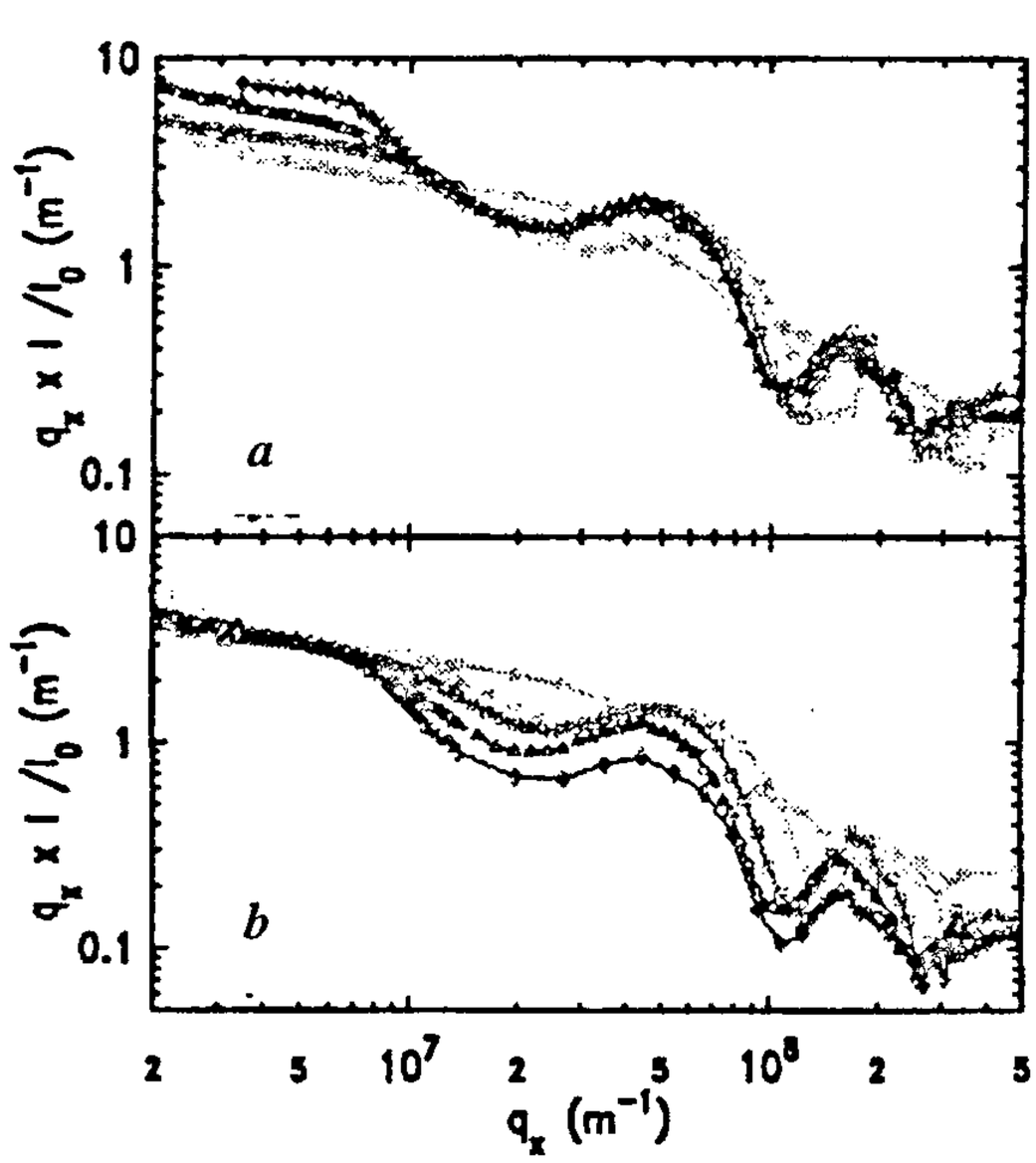

Figure 14. *a*, Intensity scattered by an arachidic acid film (dark curves) and water (faint curves). The surface tensions are (top to bottom) 33 mN/m (diamonds), 43 mN/m (triangles), 53 mN/m (squares), 69 mN/m (circles) and 73 mN/m. *b*, Same data normalized by γ/γ_{water} in order to illustrate the scaling $I \propto \gamma$ in the range $3 \times 10^6\ m^{-1} \leq q_x \leq 8 \times 10^6\ m^{-1}$ where capillary waves dominate the fluctuation spectra. The fringes are due to the normal film structure since q_z is not constant in the (x, z) configuration.

4.3. *Liquid–liquid interfaces*

Only a few X-ray reflectivity experiments at liquid–liquid interfaces have been attempted up to now (neutron reflectivity experiments will not be discussed here). In Roser *et al.*[33], the possibility of measurements using the high energy bremstrahlung of a tungsten tube was demonstrated. Two geometries are possible with the incident beam coming either through the top or the side (Figure 16). The experiment was done at a fixed angle with an energy-sensitive detector. The main difficulty is related to the transmission through the 7 cm wide cell (Figure 16, left). Quite surprisingly, this classical set-up allowed the measurement of a very nice reflectivity curve at the water–cyclohexane interface (Figure 16, right).

McClain *et al.*[34] studied a surfactant film in contact with the microemulsion middle phase in a decane, water, triethylene glycol monooctyl ether (C_8E_3) ternary mixture at 17 keV using synchrotron radiation (NSLS, beamline X20B). They measured both reflectivity (Figure 17, left) and diffuse scattering (Figure 17, right). The rms roughness extracted from the reflectivity experiment was $\langle z^2 \rangle^{1/2} = 8.5$ nm. In addition, the diffuse scattering experiment yielded $\gamma = 0.11$ mN/m and

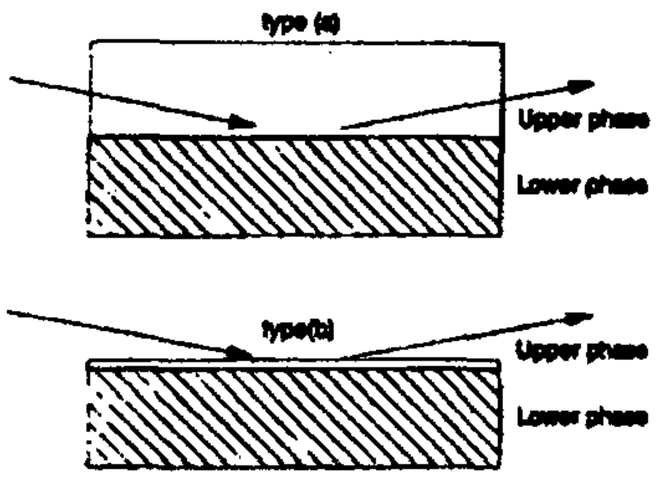

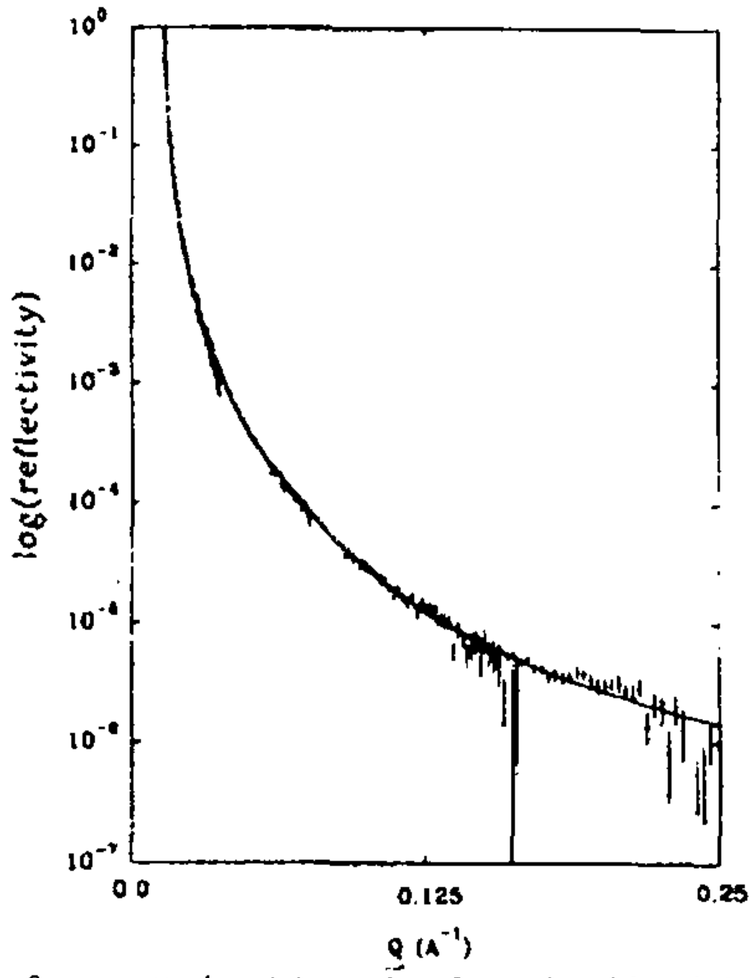

Figure 16. (Left), Possible geometries for liquid–liquid surface scattering (a) coming from the side of the upper liquid and (b) beam coming from the top of the upper liquid. (Right), Reflectivity of the water/cyclohexane interface and model fit using a Fresnel reflectivity profile with additional roughness. Adapted from Roser *et al.*[33].

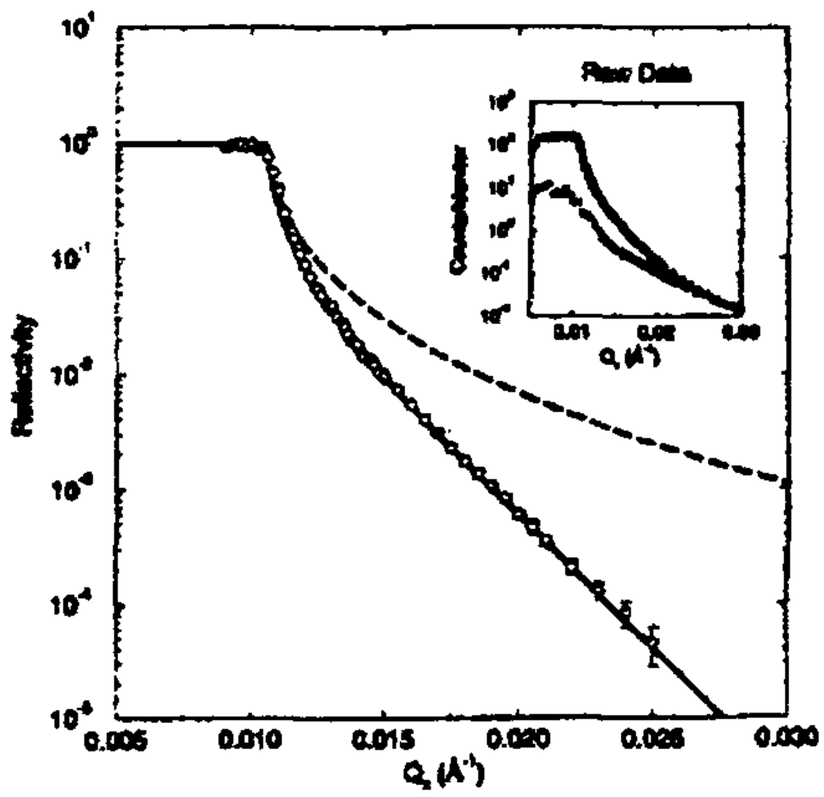

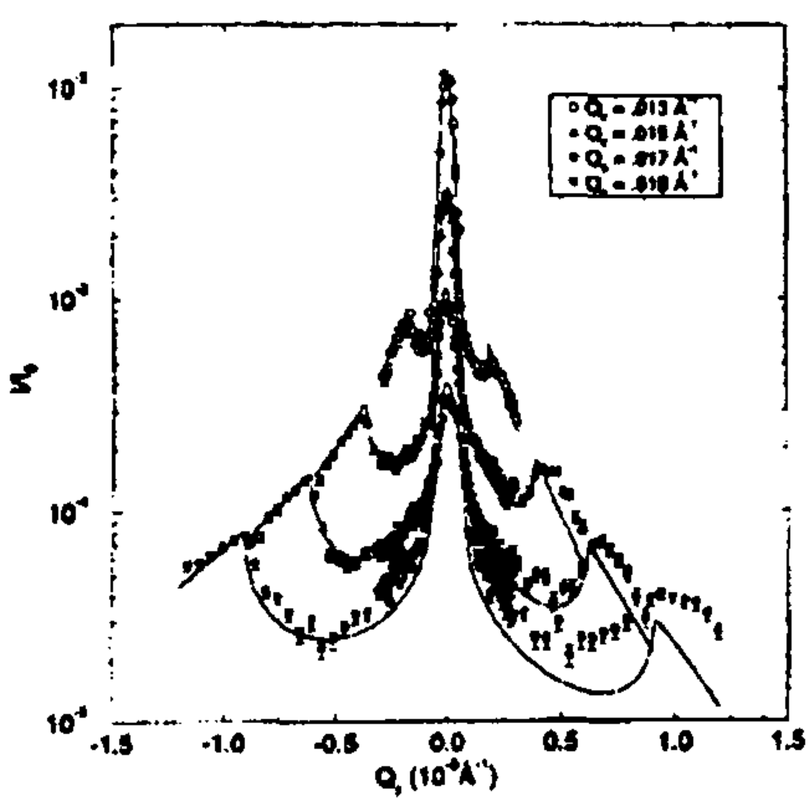

Figure 17. (Left), Specular reflectivity from the water–microemulsion interface. The dashed line is the Fresnel reflectivity of the corresponding flat interface, and the solid line is calculated with a rms roughness of 8.5 nm. Raw data (circles) and background (squares) are displayed in the inset. (Right), Diffuse scattering from the water–microemulsion interface (q_x scans at fixed indicated q_z value). The theoretical lines are calculated with a surface tension $\gamma = 0.11$ mN/m. Adapted from McClain *et al.*[34].

$K < 0.5\ k_BT$. Note however that the curves in Figure 17 suffer from background subtraction problems at large q_z values which represent in fact the main difficulty of such experiments. Another illustration of a liquid–liquid interface measurement is given in Figure 18 (ref. 35). A dedicated two-barrier Langmuir trough made of glass (lower part containing water) and teflon (upper part containing oil) to avoid leakage, equipped with very thin (50 μm) teflon windows for the X-ray beam was used. The optimal cell width resulting of a balance between absorption and the requirement of a flat meniscus is 7 cm. A high energy was used (18 keV), $\lambda = 0.068$ nm, for which the transmission through the 7 cm wide film of hexadecane is ≈ 0.1. Detector scans in the plane of incidence are represented in Figure 18. The amphiphile used is the phospholipid DPPC which forms very stable films at the water/oil interface and can therefore be compressed to high pressures (i.e. low surface tensions), thus giving rise to a large diffuse scattering signal. The fluctuations of this amphiphilic film ($\gamma = 10$ mN/m) at the oil–water interface could be measured up to wave vectors ~ 10^8 m^{-1}. The background is very large but the subtraction procedure used in this study is sufficiently efficient and reliable to allow the measurement of

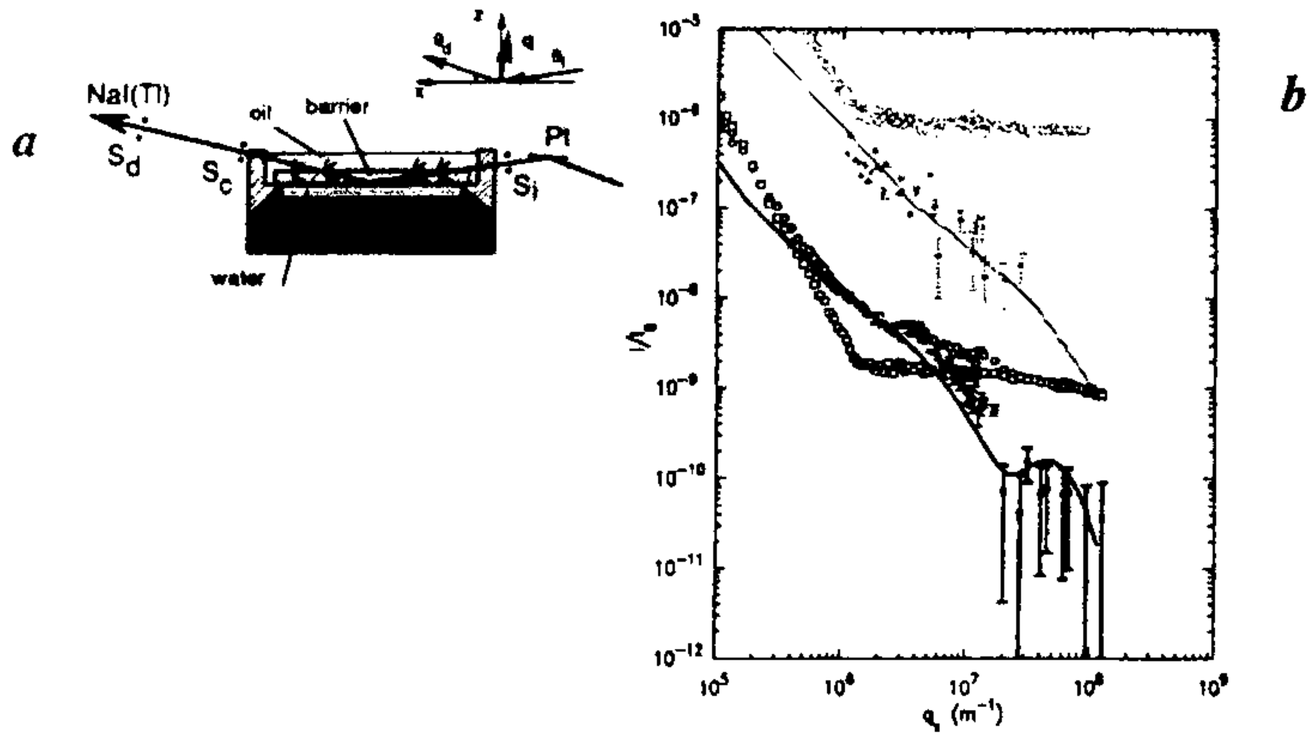

Figure 18. *a*, Schematic of the experiment (ESRF, BM32); *b*, Diffuse X-ray scattering at the hexadecane–water interface. Detector θ_{xc} scans in the vertical plane of incidence; Light symbols and curve, bare hexadecane–water interface; Dark symbols and curve, compressed L-α-dipalmytoilphosphatidylcholine film (γ = 10 mN/m). These curves are divided by a factor of 1000. Empty circles, signal; empty squares, background mainly due to bulk hexadecane scattering; filled cirles, signal minus background. Adapted from Fradin *et al.*[35].

very small signal to background ratios. The structural parameters used to analyse the data were similar to those of compressed DPPC films at the water/air interface, and the film fluctuations could be analysed using eq. (18) with γ = 10 mN/m.

As a summary, we have shown in this review that liquid surfaces can now be studied with a high precision for length-scales ranging from angströms to tens of microns using X-ray reflectivity techniques. Such techniques also give very interesting results at liquid–liquid interfaces.

1. Lu, B. C. and Rice, S. A., *J. Chem. Phys.*, 1978, **68**, 5558.
2. Bosio, L. and Oumezine, M., *J. Chem. Phys.*, 1984, **80**, 959.
3. Braslau, A., Deutsch, M., Pershan, P. S., Weiss, A. H., Als-Nielsen, J. and Bohr, J., *Phys. Rev. Lett.*, 1985, **54**, 114.
4. Braslau, A., Pershan, P. S., Swislow, G., Ocko, B. M. and Als-Nielsen, J., *Phys. Rev. A*, 1988, **38**, 2457.
5. Daillant, J., Bosio, L., Harzallah, B. and Benattar, J. J., *J. Phys. France II*, 1991, **1**, 149.
6. Schwartz, D. K., Schlossman, M. L., Kawamoto, E. H., Kellog, G. J. and Pershan, P. S., *Phys. Rev. A*, 1990, **41**, 5687.
7. Sanyal, M. K., Sinha, S. K., Huang, K. G. and Ocko, B. M., *Phys. Rev. Lett.*, 1991, **66**, 628.
8. Gourier, C., Daillant, J., Braslau, A., Alba, M., Quinn, K., Luzet, D., Blot, C., Chatenay, D., Grübel, G., Legrand, J. F. and Vignaud, G., *Phys. Rev. Lett.*, **78**, 3157.
9. Dietrich, S. and Haase, A., *Phys. Rep.*, 1995, **260**, 1.
10. Thomas, R. K. and Penfold, J., *Curr. Opin. Colloid Interface Sci.*, 1996, **1**, 23.
11. Sinha, S. K., *Curr. Opin. Solid State Material Sci.*, 1996, **1**, 645.
12. van der Waals, J. D., *Verh. K. Akad. Wet. Amsterdam*, 1893, **1**, 8.
13. Rowlinson, J. S. and Widom, B., *Molecular Theory of Capillarity*, Clarendon Press, Oxford, 1982.
14. Buff, F. P., Lovett, R. A. and Stillinger Jr F. H., *Phys. Rev. Lett.*, 1965, **15**, 621.
15. Kayser, R. F., *Phys. Rev. A*, 1986, **33**, 1948.
16. Loudon, R., in *Surface Excitations* (eds Agranovich, V. M. and Loudon, R.), North-Holland, Amsterdam, 1984, vol. 9.
17. Evans, R., *Mol. Phys.*, 1981, **42**, 1169.
18. Bourdieu, L., Daillant, J., Chatenay, D., Braslau, A. and Colson, D., *Phys. Rev. Lett.*, 1994, **72**, 1502.
19. Meunier, J., *J. Phys.*, 1987, **48**, 1819.
20. Niapórkowski, M. and Dietrich, S., *Phys. Rev. E*, 1993, **47**, 1836.
21. Helfrich, W., *Z. Naturforsch. C*, 1973, **28**, 693.
22. Daillant, J., Quinn, K., Gourier, C. and Rieutord, F., *J. Chem. Soc., Faraday Trans.*, **92**, 505.
23. Sinha, S. K., Sirota, E. B., Garoff, S. and Stanley, H. B., *Phys. Rev. B*, 1988, **38**, 2297.
24. Fukuto, M., Heilmann, R. K., Pershan, P. S., Griffiths, J. A., Yu, S. M. and Tirrell, D. A., *Phys. Rev. Lett.*, 1998, **81**, 3455.
25. Tostmann, H., DiMasi, E., Pershan, P. S., Ocko, B. M., Shpyrko, O. G. and Deutsch, M., *Phys. Rev. B*, 1999, **59**, 783.
26. Daillant J. and Bélorgey, O., *J. Chem. Phys.*, 1992, **97**, 5824.
27. de Jeu, W. H., Schindler, J. D. and Mol, E. A. L., *J. Appl. Crystallogr.*, 1996, **29**, 511.
28. Many references concerning this work can be found in Deutsch, M., Ocko, B. M., Wu, X, Z. Sirota, E. B. and Sinha, S. K., *Short and Long Chains at Interfaces* (eds Daillant, J. *et al.*), Editions Frontières, Gif-sur-Yvette 1995, p. 155.
29. Rieu, J. P., Legrand, J. F., Renault, A., Berge, B., Ocko, B. M., Wu, X. Z. and Deutsch, M., *J. Phys. II France*, 1995, **5**, 607.
30. Sackmann, E., in *Handbook of Biological Physics* (eds Lipowsky, R. and Sackmann, E.), North-Holland, Amsterdam, 1995, vol. 1A.
31. Daillant, J. and Bélorgey, O., *J. Chem. Phys.*, 1992, **97**, 5837.
32. Mol, E. A. L., Schindler, J. D., Shalaginov, A. N. and de Jeu, W. H., *Phys. Rev. E*, 1996, **54**, 536.
33. Roser, S. J., Felici, S. and Eaglesham, A., *Langmuir*, 1994, **10**, 3853.
34. McClain, B. R., Lee, D. D., Carvalho, B. L., Mochrie, S. G. J., Chen, S. H. and Litster, J. D., *Phys. Rev. Lett.*, 1994, **72**, 246.
35. Fradin, C., Luzet, D., Braslau, A., Alba, M., Muller, F., Daillant, J., Petit, J. M. and Rieutord, F., *Langmuir*, 1998, **14**, 7329.

ACKNOWLEDGEMENTS. Most of the work presented in this review has been done in collaboration with A. Braslau, M. Alba, D. Luzet, C. Fradin, C. Gourier and C. Blot at SPEC, and with F. Rieutord, G. Grübel, and D. Smilgies at the ESRF.